Journal of Hydroscience and Hydraulic Engineering
Vol.12, No.2, November, 1994, 69-84

INSTABILITY-INDUCED HORIZONTAL VORTICES IN SHALLOW OPEN-CHANNEL FLOWS WITH AN INFLECTION POINT IN SKEWED VELOCITY PROFILE

Syunsuke IKEDA, Kenichi OHTA
Department of Civil Engineering, Tokyo Institute of Technology, Meguro, Tokyo

and

Hiroshi HASEGAWA
Dengenkaihatsu KK, Ginza, Chuo, Tokyo

SYNOPSIS. Generation of periodic horizontal vortices was studied in temrs of linear stability analysis for open channel flows with an inflection point in depth-averaged velocity profile. The dimensionless angular frequency of maximum instability is found to be uniquely correlated with the ratio of two parallel undisturbed flow velocities. Periodic vortices were observed by dye injected into flow, and the period was measured with a wave gage. The theory predicts the measured period very well.

INTRODUCTION

It has been known that instability is induced for flows with an inflection point in velocity distribution (e.g., Tatsumi and Gotoh, 1989), and the instability-induced disturbance eventually grows to a discrete organized vortex. Such a phenomenon can be seen even for natural geophysical flows, e.g. for open channel-flow in compound channel, for flow in channels with laterally varying bottom roughness and for flow in rivers with bank vegetation or pile dikes.

Several studies have been made in Japan for horizontal organized vortices generated in rivers with compound cross sections, because many Japanese rivers take the compound cross section which consists of a main channel and flood plains.

Kinoshita (1978) found that large scale horizontal vortices are generated at the edge of Tone river flood plains, and some of them are large enough to reach the opposite side. Recently, Utami (1991) has observed horizontal vortices in Ishikari river employing aerial photography, from which he calculated the instantaneous velocity vectors and the streamlines at the free surface of flow. He found the cat's eye streamline system for rolled-up horizontal vortices, detecting from a frame moving with temporally-averaged flow velocity at the edge of the flood plain. Since the depth-averaged flow velocity has an inflection point near the edge of the flood plain, it is strongly suggested that these horizontal vortices are induced by the aforementioned instability.

The trains of large horizontal vortices have been observed also in laboratory compound channels. Tamai et al. (1986) measured the period of vortex generation for flows in compound channels, in which the period was found to agree reasonably well with the prediction obtained in terms of inviscid linear stability analysis for hyperbolic-tangent velocity profile (Michalke, 1964, 1965).

A comprehensive review on the stability analysis of free shear layers is found in Ho and Huerre (1984), and therefore is not repeated herein. One of the major conclusions of the linear stability analysis is that the Strouhal number for the maximum amplification rate, $f_n\theta_0/\bar{U}$, takes a nearly constant value of 0.032 for any hyperbolic-tangent velocity profile, in which f_n = natural frequency of the maximum instability, θ_0 = momentum thickness of the initial undisturbed flow and $\bar{U}$ = averaged velocity of two parallel free flows.

The lateral distribution of depth-averaged fluid velocity for shallow open channel flows is, however, usually skewed from the tangent-hyperbolic profile by the bottom friction and/or the fluid drag due to, e.g. bank vegetation or pile dikes. Instability of shallow water flow with skewed depth-averaged velocity profile is thus treated herein to predict the frequency of vortex generation at the inflection point of the velocity distribution. The results are tested with laboratory experiments to support the theory.

DEPTH-AVERAGED VELOCITY DISTRIBUTION

A straight channel with rectangular cross section is considered, for which the width and the depth are denoted by B and D, respectively. The depth is assumed to be constant throughout the flow field. The flow is retarded by vegetation or pile dikes (hereinafter they are termed VoP for abbreviation) which locate in both sides of the channel, the width of which is B_s (see Fig. 1). VoP is simulated by circular cylinders with a diameter d. They are placed in stagger with longitudinal interval, ℓ_x, and lateral interval, ℓ_y. It is assumed that the flow is uniform longitudinally, which implies that the flow is fully-developed, and therefore the longitudinal slope of free surface, S, is constant everywhere. The depth of flow is assumed to be much smaller than the lateral scales such as B and B_s, which implies that the depth-averaged shallow water treatment is allowed in analysing the flow field.

The momentum balance for flow outside of VoP region is, then, described by

$$\rho gDS + \rho\varepsilon_y D \frac{d^2\bar{u}}{dy^2} - \rho C_f \bar{u}^2 = 0 \qquad (1)$$

in which ρ = mass density of fluid, g = gravitational acceleration, ε_y = lateral eddy viscosity, assumed to be constant with respect to y, y = lateral coordinate taken positive toward VoP region from the edge of the region (see Fig. 1), $\bar{u}$ = depth-averaged local fluid velocity, C_f = a resistance coefficient defined by $(u_*/\bar{u})^2$, assumed to be constant laterally, and u_* = friction velocity. The momentum equation for flow in VoP region is

$$\rho gDS + \rho\varepsilon_y D \frac{d^2\bar{u}}{dy^2} - \rho C_f \bar{u}^2 - \rho C_D aD \frac{\bar{u}^2}{2} = 0 \qquad (2)$$

in which C_D = drag coefficient of single VoP, and $a = d/(2\ell_x\ell_y)$ = a parameter describing the density of VoP per unit area. The lateral diffusion term in Eq. 1 vanishes in the region far from VoP, and Eq. 1 reduces to

$$\rho gDS = \rho C_f \bar{u}_\infty^2 \qquad (3)$$

in which $\bar{u}_\infty$ = value of $\bar{u}$ in the lateral far field, i.e. at $y = -\infty$. Division

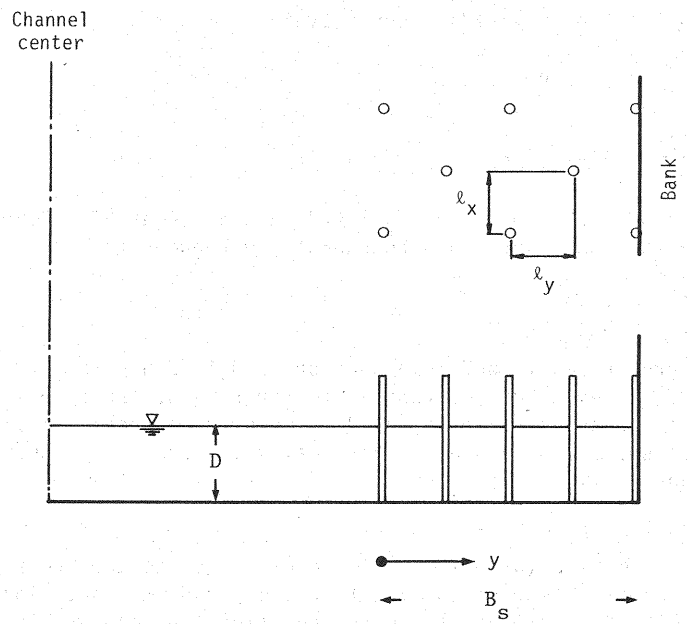

Fig. 1. Schematic view of a channel with vegetation or pile dikes and definition sketch.

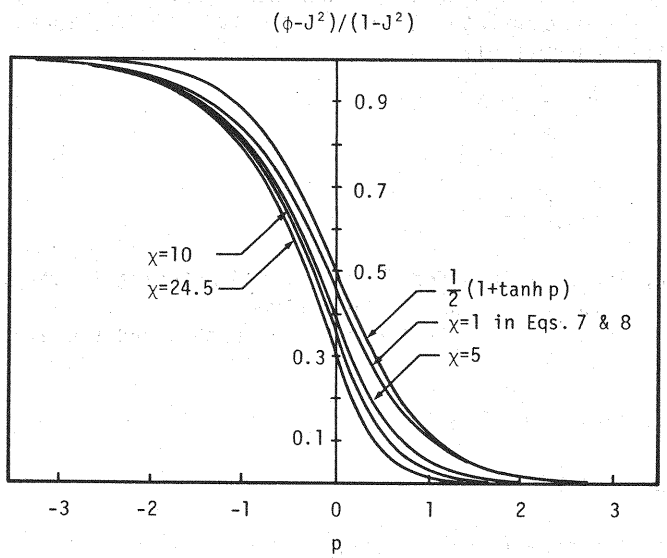

Fig. 2. Normalized velocity profiles for various values of χ. The velocity profile is anti-symmetrical with respect to p = 0 for the hyperbol tangent velocity profile, and the velocity distribution is seen become skewed as χ increases.

of Eqs. 1 and 2 by Eq. 3 yields, respectively

$$1 + \nu\frac{d^2\phi}{d\eta^2} - \phi^2 = 0 \tag{4}$$

$$1 + \nu\frac{d^2\phi}{d\eta^2} - (1+\chi)\phi^2 = 0 \tag{5}$$

in which $\nu = \varepsilon_y D/C_f \bar{u}_\infty B^2$, $\phi = \bar{u}/\bar{u}_\infty$, $\eta = y/B$, and $\chi = C_D aD/2C_f$. Since ε_y can be equated to $\alpha u_* D$ as described subsequently, ν reduces to

$$\nu = \frac{\alpha}{\sqrt{C_f}}\left(\frac{B}{D}\right)^2 \tag{6}$$

in which α = proportional coefficient of order 0.1. Since the order of C_f is 0.01 and D/B is much smaller than unity for rivers, the dimensionless velocity, ϕ, is expected to be expanded in power series of a small parameter ν to solve Eqs. 4 and 5 analytically in terms of perturbation technique. Thus, ϕ is expressed by

$$\phi = \phi_0 + \nu\phi_1 + \nu^2\phi_2 + \ldots. \tag{7}$$

in which ϕ_0, ϕ_1, ϕ_2 = solutions of ϕ in zeroth, 1st and 2nd orders, respectively. Substitution of Eq. 7 into Eq. 4 yields the solutions, $\phi_0 = 1$, $\phi_1 = \phi_2 = 0$, which are the outer solutions in term of singular perturbation, and the analysis has failed to include the diffusion terms embodied by the second term in Eqs. 4 and 5. The reason is that the diffusion terms are not small in the mixing zone but comparable with the other terms, suggesting that another inner variable scaled by "boundary layer thickness" should be introduced. Singular perturbation technique indicates that the appropriate inner variable is $p = \eta/\sqrt{\nu}$. Then, Eqs. 4 and 5 reduce to, respectively

$$1 + \frac{d^2\phi}{dp^2} - \phi^2 = 0 \tag{8}$$

$$1 + \frac{d^2\phi}{dp^2} - (1+\chi)\phi^2 = 0 \tag{9}$$

Substituting again Eq. 7 into Eqs. 8 and 9, and matching ϕ, $d\phi/dp$ and $d^2\phi/dp^2$ at $p = 0$, the solutions can be derived.

The solutions up to the first order (the second and the higher orders are truncated) read

$$\phi = 1 - (1-J)\exp\left(\frac{2}{\nu}\right)^{1/2}\eta \tag{10}$$

for the region outside of VoP, and

$$\phi = J\{J + (1-J)\exp[-\left(\frac{2}{\nu}\right)^{1/2}\frac{\eta}{J}]\} \tag{11}$$

for the region inside of VoP, in which $J = 1/(1+\chi)^{1/4}$.

The solutions up to the second order, which are required in the subsequent stability analysis, are expressed by

$$\phi = 1 - \frac{1}{3}(1-J)[4 - \exp(\sqrt{2}p)]\exp(\sqrt{2}p) \tag{12}$$

for the region outside of VoP, and

$$\phi = J\{J + \frac{1}{3}(1-J)[4 - \exp(-\frac{\sqrt{2}p}{J})]\exp(-\frac{\sqrt{2}p}{J})\} \tag{13}$$

for the inside of VoP region. Eqs. 10 and 11 (or Eqs. 12 and 13) indicate that the value of ϕ at p = 0 is given by

$$\phi_{p=0} = J \tag{14}$$

The depth-averaged dimensionless fluid velocity far inside of VoP region, $\phi_{p=\infty}$, is found to be

$$\phi_{p=\infty} = J^2 \tag{15}$$

from Eqs. 11 (or 13).

The velocity distribution is normalized by the velocity difference of two parallel streams, $\bar{u}_\infty$ and $\bar{u}_{p=\infty}$, such that

$$\Phi(p) = \frac{\bar{u} - \bar{u}_{p=\infty}}{\bar{u}_\infty - \bar{u}_{p=\infty}} = \frac{\phi - J^2}{1 - J^2} \tag{16}$$

where $\bar{u}_{p=\infty}$ is the undisturbed flow velocity in VoP region. $\Phi(p)$ is depicted in Fig. 2 for various values of the dimensionless VoP parameter, χ. The figure reveals that the velocity distribution becomes skewed as χ increases, and the inflection point exists at p = 0 regardless of the value of χ.

LATERAL EDDY VISCOSITY

Lateral eddy viscosity, ε_y, is one of the major factors for determining the velocity profile. The Prandtl's hypothesis for free turbulence is employed herein, namely

$$\tau_y = \rho\varepsilon_y\frac{\partial\bar{u}}{\partial y} = \rho\gamma\delta_{dis}(\bar{u}_\infty - \bar{u}_{p=\infty})\frac{\partial\bar{u}}{\partial y} \tag{17}$$

in which γ = a proportional constant, δ_{dis} = displacement thickness of the mixing zone defined by

$$\delta_{dis} = \frac{1}{\bar{u}_\infty - \bar{u}_{p=0}}\int_{-\infty}^{0}(\bar{u}_\infty - \bar{u})dy + \frac{1}{\bar{u}_{p=0} - \bar{u}_{p=\infty}}\int_{0}^{\infty}(\bar{u} - \bar{u}_{p=\infty})dy \tag{18}$$

The first order solutions, Eqs. 10 and 11, are employed herein to calculate the displacement thickness, because a simple expression δ_{dis} is obtained by using the first order solution and the result differs very little from that calculated from the second order solution. The result is

$$\delta_{dis} = \sqrt{\nu/2}(1+J)B \tag{19}$$

Substituting Eqs. 14, 15 and 19 into Eq. 17, ε_y reduces to

$$\varepsilon_y = \gamma\delta_{dis}(\bar{u}_\infty - \bar{u}_{p=\infty}) = \frac{\gamma^2}{2C_f^{1.5}}(1-J)^2(1+J)^4 u_{*\infty} D \tag{20}$$

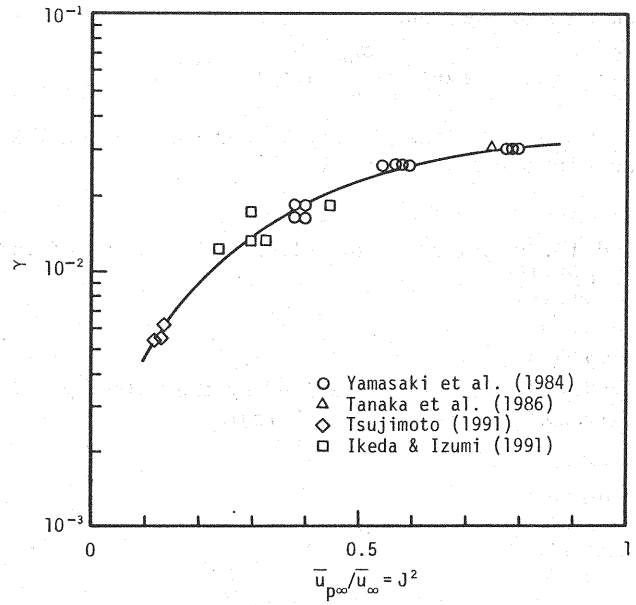

Fig. 3. Measurement of the proportional constant, γ, in Eq. 17 as a function of J^2. The solid line indicates the best fit curve expressed by Eq. 21.

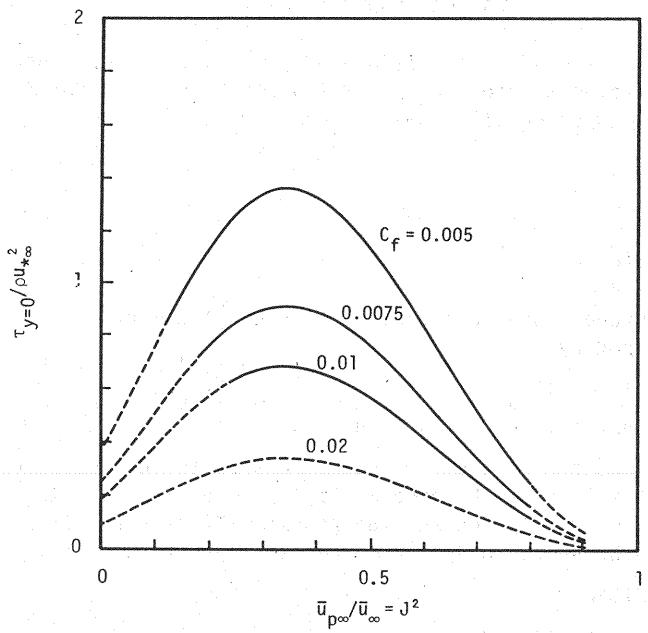

Fig. 4. Dimensionless shear stress at the edge of VoP region as a function of J^2 and C_f. It should be noted that there exists a maximum at about $J^2 = 1/3$. The broken line idicates extrapolation from the measured value.

in the derivation of which the relations, $\nu=\varepsilon_y D/C_f \bar{u}_\infty B^2$, $C_f=(u_{*\infty}/\bar{u}_\infty)^2$ and $\bar{u}_{p=\infty}=\bar{u}_\infty J^2$, are used, in which $u_{*\infty}$ is the shear velocity at $y = -\infty$. Eq. 20 indicates that the lateral eddy viscosity is proportional to $u_{*\infty}D$ for lateral mixing zone generated in shallow open channel flows, as assumed previously. The proportional constant, γ, must be determined empirically. Lateral shear fields have been produced in a wind tunnel (Tanaka et al., 1986) and in an open flume (Yamasaki et al., 1984) with laterally different bottom roughnesses and also in open flumes with circular cylinders placed along one side of the flumes (Ikeda and Izumi, 1991; Tsujimoto, 1991). The values of γ were calculated by fitting the first order solution for $\bar{u}$ to the measured distributions. The results are depicted in Fig. 3, in which it is revealed that γ is uniquely correlated with $\bar{u}_{p=\infty}/\bar{u}_\infty$ $(=J^2)$. The best-fit empirical relation, which is depicted in Fig. 3 by solid line, is described by

$$\gamma = 0.035\exp[-2.95\exp(-3.8J^2)] \tag{21}$$

Therefore, the dimensionless lateral eddy viscosity, $\varepsilon_y/u_{*\infty}D$, is a function of J(or χ) and C_f as seen in Eq. 20.

It is interesting to know the lateral shear stress at the edge of VoP region, $\tau_{y=0}$. Using again the first order solutions for $\bar{u}$ and Eq. 20 for ε_y, $\tau_{y=0}$ is calculated to be

$$\tau_{y=0} = \frac{\gamma(1-J^2)^2}{C_f}\rho u_{*\infty}^2 \tag{22}$$

Eq. 22 is depicted in Fig. 4 in dimensionless form. It is found that the shear stress takes a maximum value at about $\bar{u}_{p=\infty}/\bar{u}_\infty=1/3$, which implies that the lateral diffusive transport of longitudinal fluid momentum takes a maximum value at about $\chi = 8$. This suggests that other substances, e.g., suspended materials, dissolved oxygen, etc., will take the maximum lateral diffusive transport rate at some value of χ.

STABILITY ANALYSIS

Since the lateral distribution of depth-averaged fluid velocity has an inflection point at p = 0, a small disturbance with some wavenumber will be amplified and grow to a discrete vortex. An inviscid stability analysis is performed herein to find the wavenumber with maximum amplification rate. The following stream function, ψ', is employed to describe the two-dimensional small disturbance:

$$\psi'(x, p, t) = \mathrm{Re}\{\psi(p)\exp[ik(x-ct)]\} \tag{23}$$

in which t = time, Re = real part, $\psi(p)$ = amplitude of disturbance, k = wavenumber, c = complex phase velocity described by

$$c = c_r + ic_i \tag{24}$$

It should be noted that the variables in Eq. 23 are made dimensionless by using $B\sqrt{\nu}$ for length scale and $B\sqrt{\nu}/\bar{u}_\infty$ for time scale. Substituting Eq. 23 into two-dimensional Euler's equation, the following Rayleigh equation is derived:

$$(\phi - c)\left(\frac{d^2\psi}{dp^2} - k^2\psi\right) - \frac{d^2\phi}{dp^2}\psi = 0 \tag{25}$$

Since the disturbance should vanish at infinitely far field, the boundary

conditions are described by

$$\psi(\infty) = \psi(-\infty) = 0 \tag{26}$$

The dimensionless fluid velocity, ϕ, is given by the second order solutions expressed as Eqs. 12 and 13. Michalke (1964) employed asymptotic form of ψ at infinity to make the integration of Eq. 25 simple. A similar method is employed herein. Since $d^2\phi/dp^2 = 0$ at $p = \pm\infty$, the asymptotic forms of ψ and $d\psi/dp$ at $p = \pm\infty$ are expressed by

$$\psi \sim \exp(-kp), \quad \frac{d\psi}{dp} \sim -k\psi \quad \text{at } p \to \infty \tag{27a}$$

$$\psi \sim \exp(kp), \quad \frac{d\psi}{dp} \sim k\psi \quad \text{at } p \to -\infty \tag{27b}$$

Therefore, ψ is equated to

$$\psi \sim \exp(\int \Psi dp) \tag{28}$$

Substituting Eq. 28 into Eq. 25, the following equation is derived for Ψ:

$$\frac{d\Psi}{dp} = k^2 - \Psi^2 + \frac{1}{\phi - c}\frac{d^2\phi}{dp^2} \tag{29}$$

The boundary conditions, Eq. 26, are reduced to with the aid of Eqs. 27a and 27b,

$$\Psi(\infty) = -k, \ \Psi(-\infty) = k \tag{30}$$

Since Eq. 29 is solved numerically, the following independent variables, q and r, are introduced to make the integration domain finite:

$$q = \exp(\sqrt{2}p) - 1 \tag{31}$$

for outside of VoP region, i.e. for $p \geq 0$, and

$$r = J[1 - \exp(-\sqrt{2}p/J)] \tag{32}$$

for inside of VoP region, in which it should be noted that $q = r = 0$ at $p = 0$. Ψ can be decomposed to the real part, Ψ_r, and the imaginary part, Ψ_i, such that

$$\Psi = \Psi_r + \Psi_i \tag{33}$$

Substituting Eqs. 24 and 33 into Eq. 29, the following equations are derived with the aid of Eqs. 31 and 32:

$$\frac{d\Psi_r}{dq} = \frac{k^2 - \Psi_r^2 + \Psi_i^2}{\sqrt{2}(q+1)} + \frac{8(1-J)q(\phi - c_r)}{3\sqrt{2}[(\phi - c_r)^2 + c_i^2]} \tag{34a}$$

$$\frac{d\Psi_i}{dq} = -\frac{2\Psi_r\Psi_i}{\sqrt{2}(q+1)} + \frac{8(1-J)qc_i}{3\sqrt{2}[(\phi - c_r)^2 + c_i^2]} \tag{34b}$$

for outside of VoP region, and

$$\frac{d\Psi_r}{dr} = \frac{k^2 - \Psi_r^2 + \Psi_i^2}{\sqrt{2}(1-r/J)} + \frac{8(1-J)r(\phi - c_r)}{3\sqrt{2}J^2[(\phi - c_r)^2 + c_i^2]} \tag{35a}$$

$$\frac{d\Psi_i}{dr} = -\frac{2\Psi_r\Psi_i}{\sqrt{2}(1-r/J)} + \frac{8(1-J)rc_i}{3\sqrt{2}J^2[(\phi - c_r)^2 + c_i^2]} \tag{35b}$$

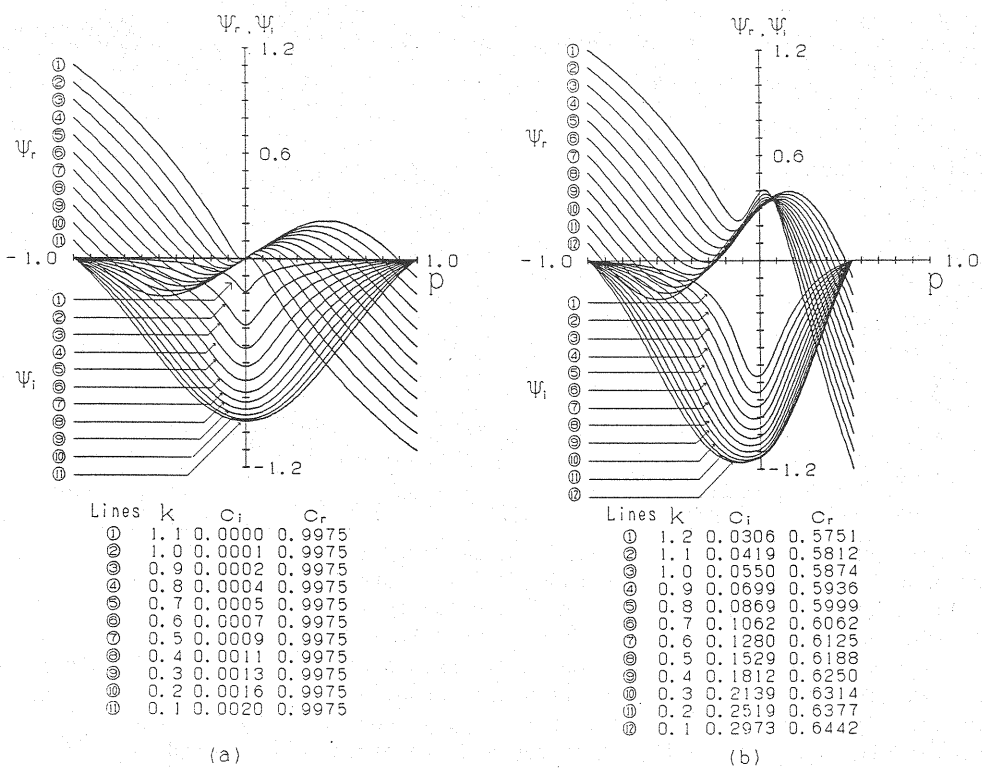

Fig. 5. Calculated eigenfunctions, Ψ_r and Ψ_i, for (a) $\chi = 0.01$ and (b) $\chi = 10$.

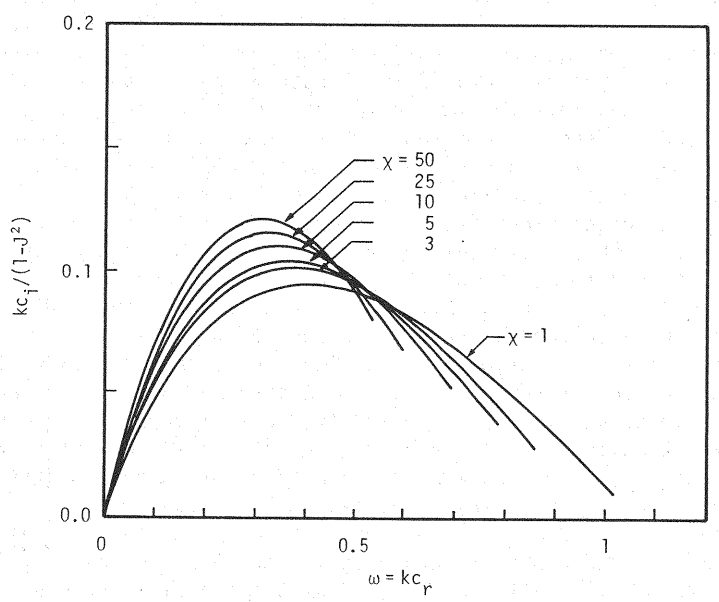

Fig. 6. Predicted growth rate of infinitesimal disturbance as a function of angular frequency, ω, and VoP parameter, χ.

for inside of VoP region. The boundary conditions are

$$\Psi_r(-1) = k,\ \Psi_r(J) = -k \tag{36a}$$

$$\Psi_i(-1) = 0,\ \Psi_i(J) = 0 \tag{36b}$$

Applying L'Hospital's rule, the derivatives of Ψ at q = -1 and r = J are given by

$$\left.\frac{d\Psi_r}{dq}\right|_{q=-1} = -\frac{8(1-J)(1-c_r)}{3\sqrt{2}(1+\sqrt{2}k)[(1-c_r)^2+c_i^2]} \tag{37a}$$

$$\left.\frac{d\Psi_i}{dq}\right|_{q=-1} = -\frac{8(1-J)c_i}{3\sqrt{2}(1+\sqrt{2}k)[(1-c_r)^2+c_i^2]} \tag{37b}$$

$$\left.\frac{d\Psi_r}{dr}\right|_{r=J} = \frac{8(1-J)(J^2-c_r)}{3\sqrt{2}J(1+\sqrt{2}Jk)[(J^2-c_r)^2+c_i^2]} \tag{37c}$$

$$\left.\frac{d\Psi_i}{dr}\right|_{r=J} = \frac{8(1-J)c_i}{3\sqrt{2}J(1+\sqrt{2}Jk)[(J^2-c_r)^2+c_i^2]} \tag{37d}$$

For antisymmetric velocity profile with respect to the inflection point, the phase velocity, c_r, is independent of the wavenumber and the velocity profile, and c_r is equated to the fluid velocity at the inflection point (Tatsumi and Gotoh, 1960). The velocity profile in the present case is nearly antisymmetric for small value of χ as depicted in Fig. 2, for which the dimensionless phase velocity is nearly equal to the dimensionless fluid velocity at the inflection point, i.e. $c_r \simeq J$ (see Eq. 14). As χ increases, the velocity profile deviates from the antisymmetric profile, and c_r becomes larger than J. In the numerical integration of Eqs. 34a - 36b under the boundary conditions, Eqs. 36a - 37d, c_r and c_i are determined for a specified value of k such that the values of Ψ_r and Ψ_i are matched at p = 0. The procedure is as follows: (1) the phase velocity is at first assumed such that $c_r = J$, (2) Ψ_i is matched at p = 0 varying c_i by trial and error, (3) c_r is changed such that the matching of Ψ_r is satisfied at p = 0, (4) this procedure is iterated until both Ψ_r and Ψ_i are matched at p = 0. In the numerical integration, Runge-Kutta-Gill scheme with a step of 0.025 was employed. It should be noted that the derivatives of Ψ_r and Ψ_i are matched automatically at p = 0 (see Eqs. 34a - 35b). Fig. 5 shows examples of the calculated profiles of Ψ_r and Ψ_i for χ = 0.01 and χ = 10. It is seen that the eigenfunctions, Ψ_r and Ψ_i, for χ = 10 are considerably skewed compared with the antisymmetric profile of Ψ_r and the symmetric profile of Ψ_i obtained for χ = 0.01. Michalke (1964) calculated the eigenfuctions, Ψ_r and Ψ_i, for the hyperbolic-tangent velocity profile which is antisymmetric with respect to the inflection point.

The result for the dimensionless amplification rate, kc_i, is depicted in Fig. 6 as a function of the dimensionless angular frequency, ω, and the VoP density parameter, χ, in which kc_i is divided by $1-J^2$ to adjust the vertical scale. The dimensionless angular frequency, ω_{max}, at which the amplification rate takes the maximum for each value of χ, can be obtained from Fig. 6, and the result is shown in Fig. 7. It is found that ω_{max} decreases slightly as increasing χ. The phase velocity at the maximum amplification rate divided by J is depicted in Fig. 8, in which it is revealed that c_r/J is gradually increased from unity as χ increases. This indicates that the phase velocity at the most amplified angular frequency is slightly above the fluid velocity at the inflection point.

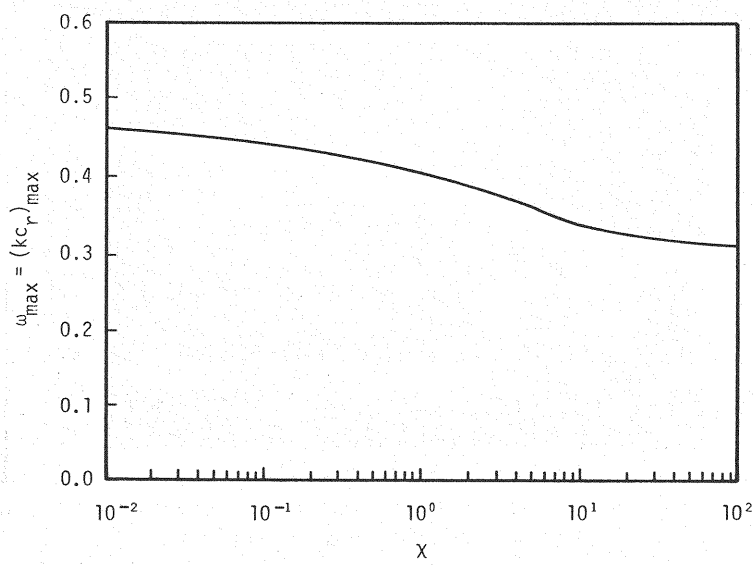

Fig. 7. Angular frequency at maximum growth rate, ω_{max}, as a unique function of χ.

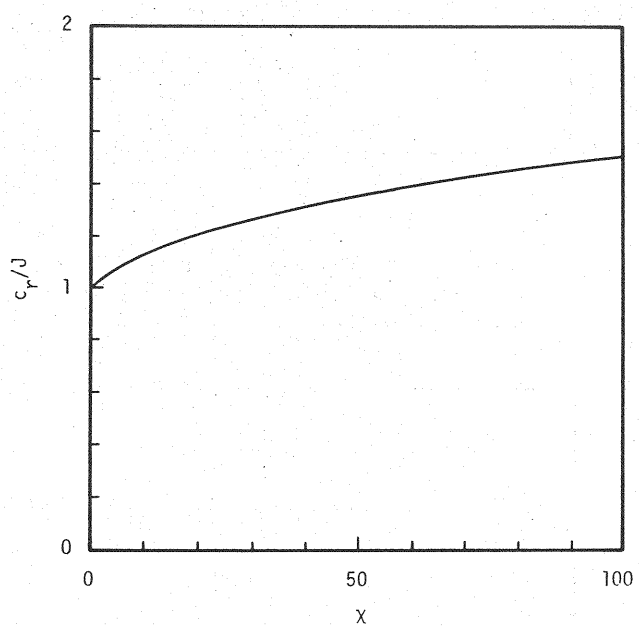

Fig. 8. Phase velocity at maximum growth rate as a function of χ. It should be noted that c_r/J increases from unity as χ increases.

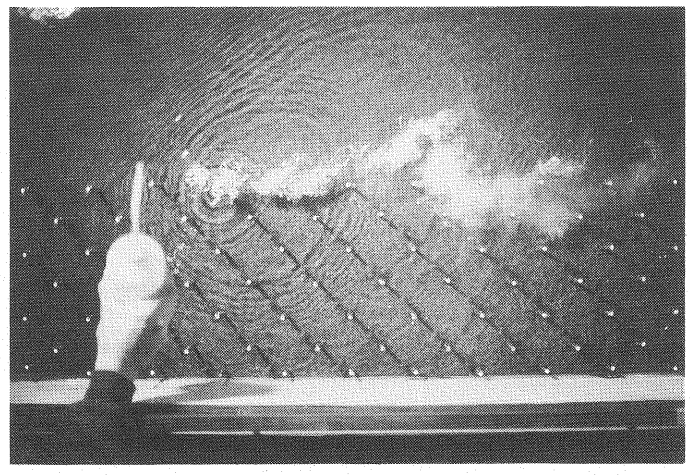

Fig. 9. Visualized organized horizontal vortex (Run 1). It is seen that the center of the vortex locates at the edge of pile region.

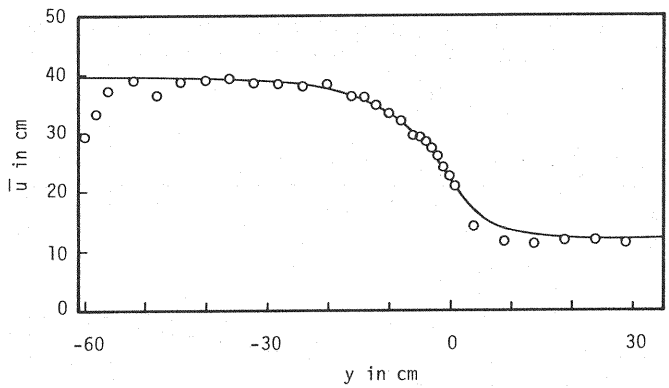

Fig. 10. Lateral distribution of depth-averaged fluid velocity (Run 1). The solid line indicates Eqs. 10 and 11.

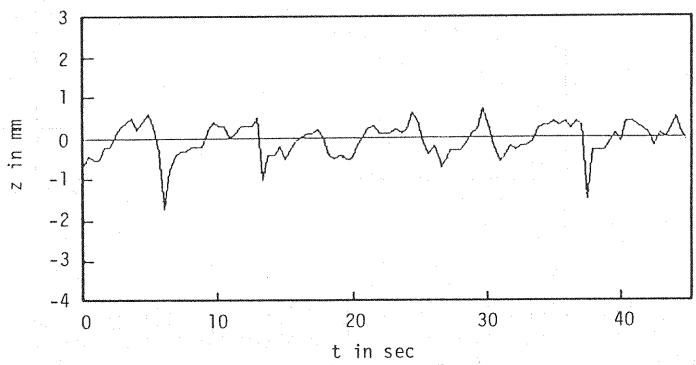

Fig. 11. Variation of free surface elevation just outside of the pile region. Water surface depresses as vortex passes through the gage.

PERIOD OF VORTEX GENERATION

As described previously, an infinitesimal disturbance with maximum amplification rate will develop to a discrete vortex as revealed by Rosenhead (1931), and the period of vortex generation is expected to be identical with that of the disturbance. Since ω_{max} is made dimensionless with a characteristic time scale of $B\sqrt{\nu}/\bar{u}_\infty$ in the present analysis, the period of vortex generation, T, is equated to

$$T = \frac{2\pi B\sqrt{\nu}}{\omega_{max}\bar{u}_\infty} \tag{38}$$

Substituting the relation, $\nu = \varepsilon_y D/C_f \bar{u}_\infty B^2$, into Eq. 38 and with the aid of Eq. 20, the reduced period, $\bar{u}_\infty T/D$, is calculated to be

$$\frac{\bar{u}_\infty T}{D} = \frac{\sqrt{2}\pi\gamma(1-J)(1+J)^2}{C_f\,\omega_{max}} \tag{39}$$

in which γ and ω_{max} are given by Eq. 21 and Fig. 7, respectively. Eq. 39 reveals that $\bar{u}_\infty T/D$ is a function of J(or χ) and C_f.

LABORATORY TESTS

The experiments were performed in a tilting straight flume with 12 m length and 0.96 m width. VoP was simulated by circular cylinders made of wood, which have a diameter of 5 mm and a length of 10 cm. They were placed in stagger with $\ell_x = \ell_y = 5$ cm. The fluid velocity was measured using a miniature propeller type velocity-meter with an outer diameter of 3 mm for 5 runs, among which Runs 1, 2 and 5 are listed in Table 1. The reason is that the period of vortex generation was measured only for the 3 runs. The number of measurements in vertical direction was 10 at each location, from the 10 measurements the depth-averaged flow velocity was calculated. The period of vortex generation was measured by a wave gage located slightly outside the edge of circular cylinder region. The facility can observe the depression of water surface induced by the vortex. The vortex was visualized by injecting white dye (poster color) into the flow from the free surface. Photographs were taken with an interval of 0.77 sec using a camera equipped with a motor-drive. An example of the photograph is shown in Fig. 9, in which a discrete vortex is seen at the edge of the circular cylinder region.

The lateral distribution of depth-averaged fluid velocity is depicted in Fig. 10 for Run 1 as an example, in which the solid line indicates the profile obtained by fitting Eqs. 10 and 11 to the measured one. The value of ε_y can be determined by the best fitting procedure, from which γ can be calculated by using Eq. 20. The result for γ depicted in Fig. 3 was thus obtained. An inflection point is observed at y = 0 (i.e., p = 0) in Fig. 10.

The variation of the free surface elevation with time is also shown for Run 1 in Fig. 11. The mean period of vortex generation was calculated by temporal averaging procedure. The periods thus obtained for three runs are shown in Table 1 along with the theoretical values predicted by Eq. 39. Since the values of dimensionless VoP parameter, χ, employed herein are relatively small (10.1 to 17.5) as documented in Table 1, the data obtained by Tsujimoto (1991) are also used herein to test the theory. His three data take χ = 50.8, 63.5 and 67.9, and therefore they have relatively large values of χ (see Table 2). A comparison between the prediction and the

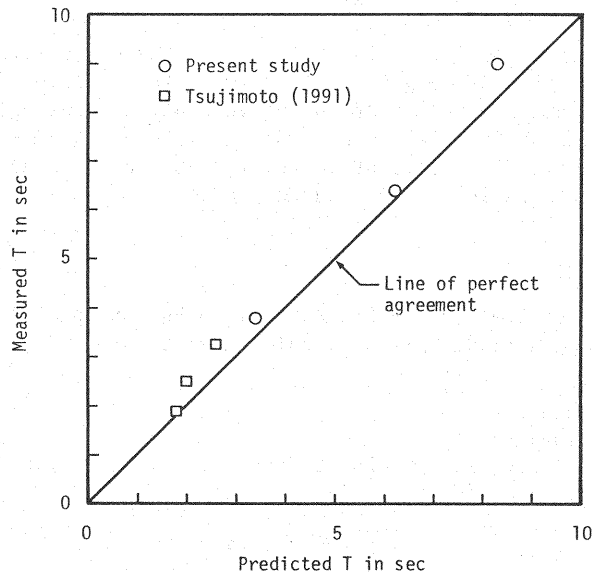

Fig. 12. Comparison of the predicted period of vortex generation with the measured period.

Table 1. Major hydraulic variables of the present laboratory tests.

Run	Q (ℓ/s)	D (cm)	S	$u_{*\omega}$ (cm/s)	$\bar{u}_{\omega}$ (cm/s)	χ	ω_{max} (Fig. 7)	Predicted T (s)	Measured T (s)
1	15.3	6.0	1/1000	2.42	31.6	10.2	0.34	6.2	6.4
2	22.6	6.0	1/300	4.43	57.3	10.1	0.34	3.4	3.8
5	23.8	8.5	1/1500	2.36	40.0	17.5	0.33	8.3	9.0

Table 2. Major hydraulic variables of the laboratory tests performed by Tsujimoto (1991).

Run	Q (ℓ/s)	D (cm)	S	$u_{*\omega}$ (cm/s)	$\bar{u}_{\omega}$ (cm/s)	χ	ω_{max} (Fig. 7)	Predicted T (s)	Measured T (s)
IW1	-	3.65	0.00148	2.31	41.5	67.9	0.31	2.6	3.3
IW2	-	3.82	0.00250	3.05	47.5	50.8	0.32	2.0	2.5
IW3	-	3.87	0.00294	3.34	57.0	63.5	0.32	1.8	1.9

measurement is shown in Fig. 12, and the agreement is found to be reasonably well. This suggests that the horizontal organized vortices generated at the edge of VoP region is induced by an instability of flow with an inflection point in velocity distribution.

CONCLUSIONS

Depth-averaged velocity distribution for open channel flow with VoP region along the banks and the associated instability of flow are studied theoretically and experimentally in the present study. The lateral distribution of the depth-averaged flow velocity is solved analytically in terms of singular perturbation. It is found that an inflection point occurrs at the edge of VoP region (at $p = 0$). The rate of lateral diffusive transport of longitudinal fluid momentum is found to take a maximum at a moderate density of VoP. The existence of inflection in the velocity distribution induces instability of flow, and the period of maximum instability for a specified wavenumber is predicted by solving Rayleigh equation. The reduced period is found to be dependent on the dimensionless density parameter for VoP, χ, and the resistance coefficient associated with bottom friction, C_f. The laboratory tests support the present analysis.

ACKNOWLEDGMENT

The present study was financially supported by the Grant-in-Aid for Scientific Research sponsored by the Ministry of Education and Culture of Japan (Grant No. 628500959), and it is also supported by Kajima Science Foundation. Valuable data were provided by T. Tsujimoto, Kanazawa University. They are gratefully acknowledged.

REFERENCES

Ho, C. M. and P. Huerre (1984) Perturbed free shear layers, Ann. Rev. Fluid Mech., 16, 365-424.

Ikeda, S. and N. Izumi (1991) Effects of pile dikes on flow retardation and sediment transport, Journal of Hydraul. Eng., ASCE, 117(11), 1459-1478.

Kinoshita, R. (1978) Field observations of flood flow and river channel pattern, JSCE Hydraulic Eng. Series 78-A-7 (in Japanese).

Michalke, A. (1964) On the inviscid instability of hyperbolic-tangent velocity profile, J. Fluid Mech., 19, 543-556.

Michalke, A. (1965) Vortex formation in a free boundary layer according to stability theory, J. Fluid Mech., 22(2), 371-383.

Rosenhead, L. (1931) The formation of vortices from a surface of discontinuity, Proc. Roy. Soc. London A134, 170-192.

Tamai, N., T. Asaeda and H. Ikeda (1986) Study on generation of periodical large surface eddies in a composite channel flow, Water Resour. Res., AGU, 22(7), 1129-1138.

Tanaka, M., T. Ishikawa and S. Kimura (1986) Lateral turbulent diffusion in parallel flows, Proc. 41st Ann. Meeting, JSCE, Part II, 295-296 (in Japanese).

Tatsumi, T. and K. Gotoh (1960) The instability of free boundary layers between uniform streams, J. Fluid Mech., 7, 433-441.

Tatsumi, T. and K. Gotoh (1989) Hydrodynamic stability theory (5th edition), Sangyo Tosho KK, Chiyodaku, Tokyo, 47-73 (in Japanese).

Tsujimoto, T. (1991) Open channel flow with bank vegetation, KHL Communication No. 2, Dept. Civil Eng., Kanazawa Univ., Kanazawa, 41-54 (in Japanese).

Utami, T. (1991) On large-scale vortices found in flood flow, Proc. 23rd Symp. on Turbulent Flow, Japan Soc. Fluid Mechanics, p. 29 (in Japanese).

Yamasaki, S., T. Ishikawa and T. Kanamaru (1984) Experimental study on open channel shear flow, Proc. 39th Ann. Meeting, JSCE, Part II. 473-474 (in Japanese).